Modeling the robotic manipulation of woven carbon fiber prepreg plies onto double curved molds

a path dependent problem

Krogh, Christian; Glud, Jens Ammitzbøll; Jakobsen, Johnny

Modeling the robotic manipulation of woven carbon fiber prepreg plies onto double curved molds: a path dependent problem

Christian Krogh[1], Jens A. Glud[1] and Johnny Jakobsen[1]

Abstract

This paper investigates the behavior of woven prepreg plies being placed on a weakly double curved mold by a robot. It is essential that the draped configuration is free from wrinkles. The baseline is a Virtual Draping Environment (VDE) that can plan and simulate robot draping sequences. It consists of a kinematic mapping algorithm for obtaining target points for the grippers on the mold surface. A simple motion planner is used to calculate the trajectories of the grippers. Here, two conceptually different draping strategies are employed. Finally, the two generated draping sequences are simulated using a transient, nonlinear Finite Element (FE) model and compared w.r.t. their predicted wrinkle formations. Material data is obtained by means of tension, bias-extension and cantilever tests. The numerical examples show that the VDE can aid in developing the automatic draping system but that the generation of feasible draping sequences is highly path dependent and non-trivial.

Keywords

Prepregs, draping, finite element modeling, kinematic modeling, automation

Introduction

Laminated prepreg composites are widely used in the aerospace industry because of their superior mechanical properties. A significant amount of the total cost relates to the manufacturing where e.g. the draping process is accomplished by means of manual labor. Draping concerns the placement of the uncured fabric in a mold. Here, it is essential that the fabric is positioned correctly and is free from wrinkles. Currently, prepreg reinforcement is draped automatically in the industry by means of Automated Tape Laying (ATL) and Automated Fiber Placement (AFP). These methods are, however, restricted to unidirectional prepreg[1]. For components designed with woven fabric as is frequently seen in the aerospace industry, it is of interest to develop an automatic layup solution that can directly substitute the current manual operation. To this end, an understanding of the fabric behavior and computer models of the draping process is needed.

Shearing (or trellising), i.e. rigid tow rotations at the cross-over points, has long been recognized as the most important deformation mechanism when initially flat fabric is deformed on a double curved mold[2]. Here, the stiffness is several orders of magnitudes lower than the fiber direction stiffness of the fabric. Recently, the out-of-plane bending stiffness has been identified as important for the formation of wrinkles and their shape[3].

The fabric response in shear and tension is the baseline for the early fabric forming models such as the work by Womersly[4] from 1937 and the *pin-jointed net model* by Mack and Taylor[5] from 1956. Here, the fibers are considered inextensible while the shear stiffness is zero. The model is quick to evaluate but it is only an idealization of the

draped configuration. This type of model is denoted a *kinematic model* as opposed to *mechanical models* which are often accomplished using the Finite Element (FE) method whereby the physics of the material can be taken into account.

One approach within the framework of mechanical models is to consider the fabric as a continuum and use homogenization theory to obtain anisotropic material properties dependent on the fabric deformation. The material model is usually implemented in standard finite elements such as shells. The material properties should preferably be related to experimental data in some way. This was e.g. neatly accomplished by Aimene et al.[6] who used a hyperelastic potential composed of contributions from fiber tensions and shear. The energy contributions were formulated as polynomials in invariants which were fit to experimental data. The use of invariants facilitated easy calculation of the constitutive law. Other continuous models are also described in the literature[7,8].

A second mechanical model approach is known as *discrete modeling*. By means of structural finite elements such as trusses, beams and membranes possibly in combination with springs the focus is to model the unit cell of the fabric. E.g. the prepreg fabric model by Skordos et al.[9] uses a grid of truss element with a bilinear material law to model the tows and nonlinear elastic-viscoplastic diagonal truss

[1]Department of Materials and Production, Aalborg University, Denmark.

Corresponding author:
Christian Krogh, Department of Materials and Production, Aalborg University, Fibigerstrade 16, 9220 Aalborg, Denmark.
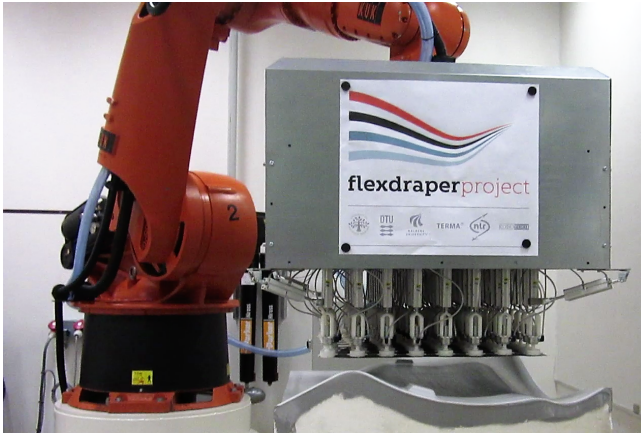Email: ck@mp.aau.dk

Figure 1. The FlexDraper robot cell. The grid of grippers is in the initial configuration over the mold after the ply has been picked up.

Figure 2. The design of the robot tool grid with actuated suction cups connected by interlinks.

elements to model the shear behavior governed by the resin. Other discrete models can also be found in the literature [10–12]. The main disadvantage is that a high number of Degrees of Freedom (DOF) usually is needed. Also, the generation of the mesh requires some attention.

Finally, a semi-discrete model, which can be considered as a hybrid between continuous and discrete, was introduced by Hamila et al. [13] in a self made special purpose finite element. The element was found efficient and easy to relate to experimental data.

The fabric forming models presented above are in many cases used to simulate the deep drawing or press forming of fabrics. The present work takes basis in a newly developed robot system for handling and draping entire prepreg plies onto weakly double curved molds. As it will be shown, the problem is highly path dependent. That is, the draped configuration including possible defects is dependent on the path taken by the robot. Determining a feasible draping sequence from the vast solution space of possible sequences is crucial and relies on modeling. The next section gives an overview of the robot system and the requirements to the modeling. Then, the *Virtual Draping Environment* is presented where kinematic and mechanical based modeling are combined to plan and simulate the draping process. Hereafter, material characterization is employed to provide material data input, and a model validation and a further numerical exploration of the path dependency is presented. Finally, the paper is concluded with a discussion.

Problem Specification

The work presented in this paper is part of the FlexDraper research project, which is briefly introduced in the following. As described in the previous section, the scope of the project is to drape entire prepreg plies onto double curved molds by means of an industrial robot. The project focuses on *weakly double curved* molds, i.e. molds without tight corners, where the plies can be readily draped without the need for post treatment and where the shear angles remain below the locking angle. The robot cell under development is depicted in Figure 1.

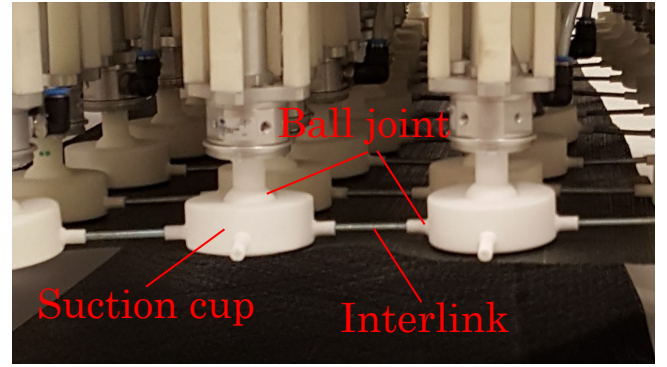The robot end effector (Figure 2) consists of a grid of vertically actuated suction cups which will be denoted

as *grippers*. The actuators are mounted in universal joints meaning that the horizontal degrees of freedom (DOF) are free. To add constraints, so-called *interlinks* are mounted between the grippers. These bars, mounted in ball joints, maintain the distance between the grippers (also mounted in ball joints) while allowing the grid to shear. Notice, that this setup entails, that only the vertical DOF are controllable.

Measures to evaluate the quality of drapes include a prescribed ply boundary and checks on the fiber angles at certain locations. Naturally, the draped plies must follow the mold surface within tight tolerances (dependent on the industry and product) and be free from wrinkles and air pockets. In the robot cell these checks will be carried out by a vision sensor system but ideally the modeling should detect possible flaws at an earlier stage.

The material system used in this study is a balanced carbon fiber 4-harness satin weave with a Bismaleimide (BMI) resin. The thickness is 0.3 mm and the areal density is 314 g/m^2. The robot system is operated at room temperature, for which reason the temperature dependency of the prepreg is neglected. All experimental work is therefore carried out at room temperature. The resin state could also influence the results. In the present study, the material was used within the processing window specified by the manufacturer.

In this study a self designed 450 mm $\times$ 450 mm double curved mold is used. It has concave and convex parts which will challenge the draping. The mold surface is defined by a 3rd degree polynomial surface:

$$z(x,y) = 1.004x + 1.089y - 3.667x^2 - 4.4x\,y -$$
$$3.75y^2 + 3.086x^3 + 8.889x^2\,y + 4.321y^3 \quad (1)$$

Here $x \in [0, 0.45]$, $y \in [0, 0.45]$. Using manual layup it was checked that a ply can be draped onto the mold, see Figure 3.

If a ply can be draped manually onto a mold, one could think it is a trivial task to determine the corresponding robot draping sequence. However, the first attempts with the system under development contradicts this statement. This is exactly the motivation for studying the problem numerically.

The Virtual Draping Environment

The Virtual Draping Environment (VDE) consists of three components depicted in Figure 4: A kinematic mapping algorithm for generating gripper target points on the mold surface, a motion planner to calculate the trajectories from
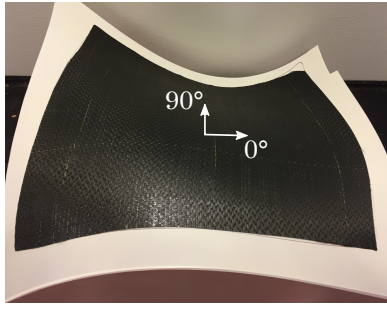
Figure 3. The mold used in this study with a manually draped ply on top. The Gaussian curvature range between -25 m^{-2} and 23 m^{-2}.
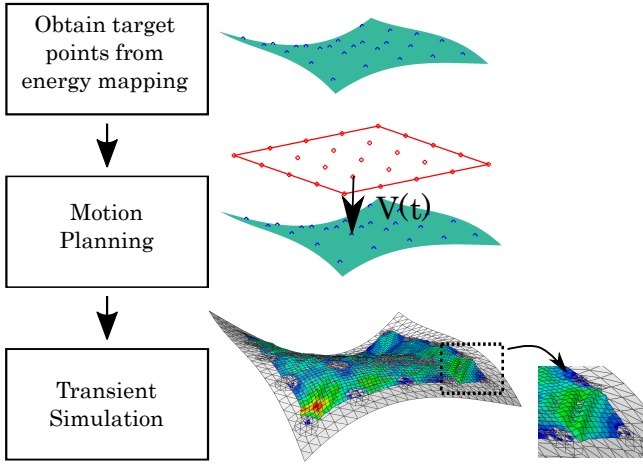

Figure 4. The components of the Virtual Draping Environment.

the initial configuration of the grippers to the target points and a transient nonlinear Finite Element (FE) model to simulate the draping sequence. The three components are elaborated in the following.

Energy Mapping Algorithm

When the draping process is carried out manually, the boundary of the final geometry is used to guide the ply, e.g. as a laser projection on the mold. This is usually given with the part specification. With the new robot tool, the ply is gripped inside the boundary which is why additional information must be calculated.

The energy mapping algorithm is a purely kinematic model that can determine the map Ψ from the flat ply in $\mathbb{R}^2$ to the draped configuration on the mold in $\mathbb{R}^3$:

$$\{x_{mold}, y_{mold}, z_{mold}\} = \Psi(x_{ply}, y_{ply}) \qquad (2)$$

The basic assumptions are that the fiber extensional stiffness is infinite and the fabric shear stiffness is zero as proposed by Mack and Taylor[5]. From large deflection shell theory it is known that tensile membrane strains develop when an initially flat sheet undergoes deformations to a finite Gaussian curvature[14]. This phenomenon is not accounted for. However, as the fabric contains voids and the model is an approximation, the approach is considered valid.

The algorithm used in this study was introduced by Bergsma and Huisman[15] and later benchmarked[16]. The ply is discretized into four node quadrilateral elements with a bilinear interpolation. The ply nodes are treated in the mold
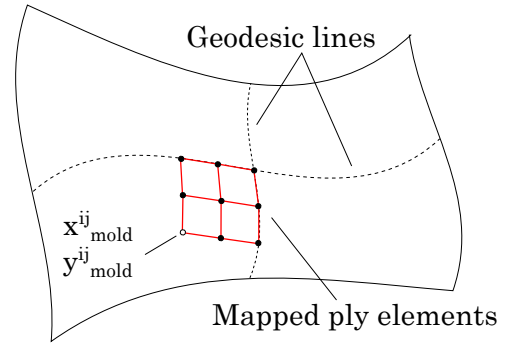

Figure 5. Energy mapping algorithm.

coordinate system. The algorithm is initiated at a chosen starting point along with two geodesic lines on the mold surface in the direction of weft and warp fiber angles. This will form a starting point from which the ply elements can be mapped The setup is depicted in Figure 5. The elements are mapped one at the time. For each element mapping, three nodes will be constrained and the free node $x_{mold}^{ij}, y_{mold}^{ij}$, is located by minimizing the fiber strain energy U which is the equivalent of minimizing the fiber strain integrated over the element volume:

$$U(x_{mold}^{ij}, y_{mold}^{ij}) = \int_V \frac{1}{2}\left(\varepsilon_{xx}^2 + \varepsilon_{yy}^2\right)\mathrm{d}V \qquad (3)$$

While this type of model has been superseded by more advanced nonlinear FE models for simulation of industrial draping processes, its application in this context is still valid. The slippage of crossing tows is small for carbon/epoxy prepregs as reported by Laroche and Vu-Khanh[17]. The same authors reported fine agreement between the experimental data and the calculations using the pin-jointed net model. Also, the shear angles remain below the locking angle (here $\approx 35°$ shear strain). However, as will become evident in the paper, shear angles below the locking angle does not necessarily alleviate wrinkles.

Once the map has been determined, the gripper target points on the mold surface can be calculated. That is, the coordinates of the grippers in the initial flat configuration can be mapped onto the mold in the final draped configuration.

Motion Planning

With information about the grippers in the initial configuration and in the final configuration, gripper trajectories can be generated. While there are infinitely many ways to construct a trajectory from one point in space to another, a starting point, which is used in this study, is a linear interpolation. That is, each gripper will move with a constant velocity in a straight line from the initial point $\mathbf{P_1}$ to the final point $\mathbf{P_2}$.

The next concern is the pattern in which the grippers are to move. Certain features in the mold may influence in what order different areas of the ply preferably should be draped[18]. From the hand layup process it is observed that the operators tend to choose some initial contact point, e.g. a corner, from which the ply is draped in a droplet or wave pattern. The immediate benefit of this approach is the avoidance of entrapped air between the mold and the ply. In this study the applicability of the VDE will be investigated by two different gripper move patterns or *draping strategies*:
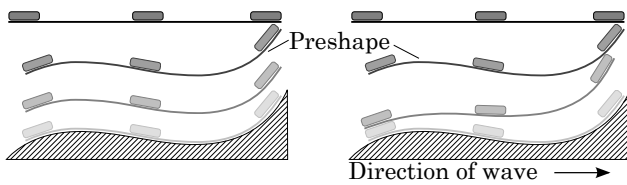
Figure 6. Draping strategies. Left: uniform draping, right: wave shape draping.
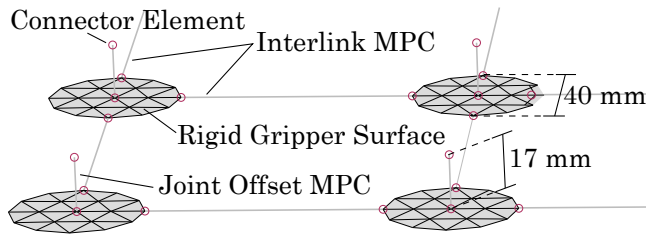

Figure 7. Modeling of interlinks and joint offset using Multi Point Constraint (MPC) elements in Abaqus. The attachment of connector elements is also shown.

1. Uniform draping, where all grippers move to the mold simultaneously.
2. Wave shape draping, where groups of grippers with equal distance to some starting point sequentially move to the mold.

To further improve the draping, a so-called *preshape* is employed: Before the draping strategy is executed, the grippers are first moved vertically such that they have equal distance to their respective target points on the mold. The principles in the two draping strategies are depicted in Figure 6 for a 2D case with three grippers.

Note that the interpolation approach does not include any information about the ply in the states between the initial configuration and the draped configuration. The approach is used as a starting point, but as will become evident in the results section, it does not necessarily lead to feasible draping sequences.

Transient Nonlinear Finite Element Model

The simulation of the generated draping sequences is carried out using Abaqus Explicit. The model comprises the ply, the mold surface and the contact surfaces of the grippers. The mold and the grippers are treated as rigid whereas the ply is modeled using the Abaqus intrinsic *fabric* material model with nonlinear, rate-depedent behavior. The input to the material model is determined in the next section. The interlinks between the grippers and the offset rotation point of the grippers are modeled by means of Multi Point Constraint (MPC) rigid beam elements as seen in Figure 7. Connector elements are introduced in the gripper rotation points in order to model a maximum and minimum rotation as well as the actuators and their mounting in the universal joints (two connector elements per gripper).

The phenomenological fabric material model is suitable for woven fabric materials where the weft and warp direction will change during deformation such that they are no longer perpendicular. It allows for capturing the in-plane deformation behaviors, i.e. fiber extension, fiber compression and shear. It is assumed that all deformation modes are decoupled. The model uses nominal stress and strain data at different strain rates as the constitutive law which is convenient to obtain. In the "Material Characterization" section it becomes evident that an increasing strain rate in general makes the ply response stiffer, i.e. a direct effect of the resin viscosity. Naturally, the model must be used in a geometric nonlinear, finite strain analysis. The outputs include the angle between the weft and warp direction, i.e. the fabric shear strain [19].

The ply is meshed with 4-node shell elements with reduced integration and hourglass control. The plate theory on which the element formulation is based, assumes a first order shear deformation through the thickness. Later in the paper it will be shown, that the shear deformation is an important part of the out-of-plane response. Another point to note regarding the out-of-plane behavior is the fact that it is obtained from the in-plane properties. This is indeed a valid assumption for homogeneous materials, but incorrect for heterogeneous materials like woven fabric. A number of remedies are proposed in the literature of which two are considered in the following due to their ease of implementation.

Döbrich et al. [20] suggested to introduce three fictitious layers in the shell. The middle layer accounts for the extensional stiffness while the outer layers account for the bending stiffness. In this way the extension and bending are conveniently decoupled and the approach is readily implemented in commercial FE softwares. This approach is valid as long as the axial stiffness of the outer bending layers is much lower than the axial stiffness of the middle extension layer. During characterization of the fabric material in this study, it was found that it exhibits a highly rate dependent behavior in bending. At high strain rates, the bending stiffness becomes significant, for which reason the decoupling is not practical.

The second approach involves adjusting the compressive stiffness in order to get the right bending behavior which causes the effective modulus to be asymmetric [21,22]. This approach is justified by the fact that relative fiber movement is possible within the tows (both in-plane and out-of-plane). Thus, the compressive stiffness is different and in general lower than the tensile stiffness of the fibers. The downside is that the bending stiffness changes if the ply is subjected to tension. In the present study, however, the bending response is mostly of concern when the ply is sagging. The asymmetric modulus approach is adopted in the present study and details are presented in the section "Cantilever Test".

The interface between the grippers and the ply involves the effects of the suction and the frictional resistance which is highly governed by the tackiness of the resin. During the initial testing on the robot system, it was found that the frictional resistance is substantial since grippers push into the ply when picking it up. With the suction on, the ply is kept fixated. Therefore, the grippers in this study are tied to the ply, i.e. modeled as having infinite friction. This approach will constrain the ply material and in reality some deformation underneath the grippers is expected.

In the interface between the ply and the mold, sliding is much more likely to occur. Here, the frictional resistance is approximated by an experimentally determined coefficient of

friction of 1.50. The experimental setup was analogous to ASTM Standard D 1894.

By default, the transient FE model is undamped for which reason damping needs to be introduced. In this study, viscous Rayleigh damping is applied due to its numerical advantages. This means, that the damping matrix equals the mass matrix scaled by some constant α. To this end, a value of α that will critically damp the system is desired, i.e. with $\zeta = 1$ in the following formula[23]:

$$\alpha = 2\zeta\omega_1 \tag{4}$$

Here ω_1 is the fundamental eigenfrequency of the system. In the following, the damping behavior is studied by means of a cantilever specimen. The setup is analogous to what will be presented in the section "Cantilever Test" where the out-of-plane properties of the prepreg is characterized. Here, the idea is to get an approximate value of α to be used in the FE models.

The frequency ω_1 of the cantilever specimen can e.g. be found by conducting an FE analysis with an undamped ply or approximated from the analytical solution to the dynamic differential equation of the beam. Here, the latter is considered. For linear elastic, isotropic materials, the fundamental eigenfrequency of a beam is given as[23]:

$$\omega_1 = 1.875^2 \sqrt{\frac{E_{static}I}{mL^3}} \tag{5}$$

In the formula E_{static} is Young's modulus, I is the moment of inertia, m is the mass of the beam and L is the length. Naturally, this formula can only approximate the fundamental eigenfrequency of a prepreg specimen, as the material cannot be considered linear elastic and isotropic. The unknown quantity in Eq. (5), E_{static} is determined as follows. From the experimental results in the "Cantilever Test" section, the static deflection of a prepreg cantilever specimen is found. Next, an isotropic, large deflection beam is fitted to the experimental static deflection by adjusting Young's Modulus. The resulting value of Young's Modulus is equal to E_{static}. Inserting the values in equation (5) the result is $\omega_1 = 11 \text{ s}^{-1}$ and by using equation (4) the damping factor becomes $\alpha = 22$. This value is obviously highly model dependent but it will used as a starting point for other analyses.

In the analyses, dynamic effects are small and thus mass scaling is applied to reduce the computation time. The mass is scaled with a factor up to 20. To this end it is checked that the kinetic energy is low compared to the strain energy in the model and that mass scaling does not alter the end result significantly for this kind of problem.

Material Characterization

This section presents the experimental tests carried out to obtain material data for the Finite Element (FE) model. These encompass tension tests for the fiber direction response, bias-extension tests for the shear response and cantilever tests for the bending response.

All tests were conducted at room temperature on a single ply with the material defrosted accordingly. Tension and bias-extension tests were conducted on an Instron 5568

electromechanical tensile test machine. A source of error which applies to all the tests is the fact that the specimens were cut to fixed dimensions which potentially involves cutting into the tows.

Tension Test

Strips of prepreg material with a width of 25 mm were cut in the fiber direction. The desired gage length is 150 mm. The strips were mounted in the grippers of the tensile test machine which was operated in displacement control until a maximum load of 500 N. Two different crosshead rates were tested: 2 mm/min and 0.5 mm/min.

The specimen deformation should ideally be obtained from a direct measurement, e.g. an extensometer or strain gage, but due to the inhomogeneity of the material this is not practical. Multiple authors have reported successful use of an optical measuring technique, such as Digital Image Correlation (DIC)[24,25]. The use of DIC was found challenging due to gaps between tows opening and closing during deformation which inhibits the correlation process. To overcome the issues it was decided to use a *compliance compensation* procedure for the tension tests. The system compliance of the tensile test machine was measured by conducting three tests on a steel specimen (grade S355) with a rectangular cross section of 25 mm $\times$ 5 mm and a gage length of 50 mm. This specimen has a stiffness several orders of magnitude higher than the prepreg strips. The specimen was mounted in the same grippers as were used for the prepreg material. At an applied load of 500 N, the theoretical elongation of the steel specimen is:

$$\delta = \frac{FL}{EA} = 0.0012 \text{ mm} \tag{6}$$

Here the value of Young's Modulus is assumed to be $E = 200$ GPa. In turn, the maximum displacement of the cross head was 0.1 mm. Thus, the elongation of the steel specimen can be neglected and the response is a measure of the test machine compliance. For reference, the maximum elongations measured during testing of the prepreg were in the order of 1 mm.

The force-displacement data of the steel specimen are subtracted from the force-displacement data of the prepreg. Next, the compliance compensated prepreg data are converted to nominal stress and strain as follows:

$$\sigma = \frac{F}{A_0} \qquad , \ \varepsilon = \frac{\Delta L}{L_0} \tag{7}$$

Here the subscript 0 indicates a quantity in the initial undeformed state. The results are presented in Figure 8.

From the figure it is seen that the prepreg material shows a non-linear stress-strain behavior. This is expected since the tows are crimped in the unloaded state and will gradually de-crimp during loading. It is also evident that the response is rate dependent which can be accredited to the presence of the resin and its straining during decrimping of the tows. As a simplification in the FE model, it is assumed that the fiber response is rate-independent. This is justified by the fact that shearing is the predominant deformation mechanism during forming. For the FE model input, the stress-strain response obtained at 2 mm/min is used.
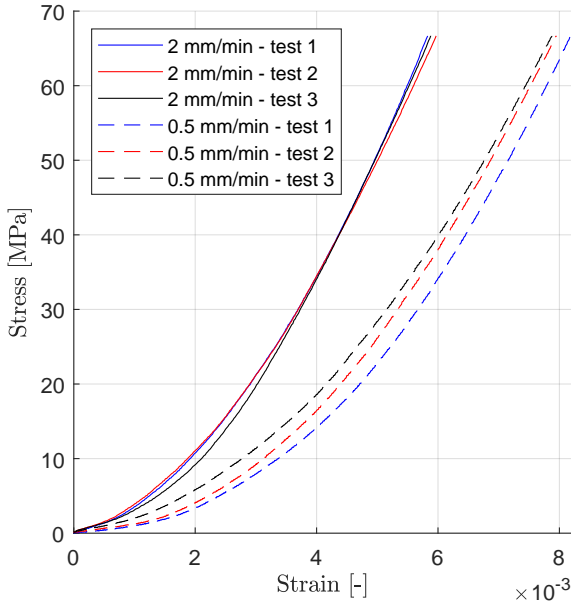
Figure 8. Nominal stress-strain response of prepreg material in the 0° direction.

Figure 9. Force vs. crosshead displacement for bias-extension tests.

Bias-extension Test

The bias-extension test is a common method for measuring the shear response of fabric. Various authors have benchmarked this test against another method, the picture frame test [26,27]. The bias-extension test was chosen based on the aforementioned benchmarks due to its simplicity and ease of application.

In the test, a wide sample of the prepreg material with fibers in ±45° is clamped in grippers at the top and bottom. When the height is at least twice the width, a pure shear zone will theoretically exist in the middle. For this study the width is 120 mm and the desired gage length is 270 mm. The tensile test machine is operated in displacement control at three different cross head rates: 2 mm/min, 10 mm/min and 100 mm/min. The results are presented in Figure 9.

The figure shows families of curves with three distinct parts: First, a steep part (≈ 0°-10° in 100 mm/min test), then a plateau (≈ 10°-35° in 100 mm/min test) and finally another steep part (≈ 35°-50° in 100 mm/min test). The first steep part corresponds to in-plane fiber bending where the tows remain fixed at the cross-over points [28]. When the frictional resistance at the cross-over points is exceeded, the tows begin to rotate and thus, the response is governed by friction effects. This corresponds to the plateau part. When neighboring tows come in contact and change cross-sectional shape, the force increases and the *locking angle* is eventually reached [29]. This is evident as the final steep part. Throughout the entire deformation intra-ply slippage is possible. As previously noted, the resin helps to keep the tows in place. Also, reports in the literature show that slippage is small below 40° shear [30,31]. Assuming three distinct shear zones in the sample (see Figure 10), a relation between the cross head movement δ and the shear angle γ in the pure shear zone, C can be derived [26]:

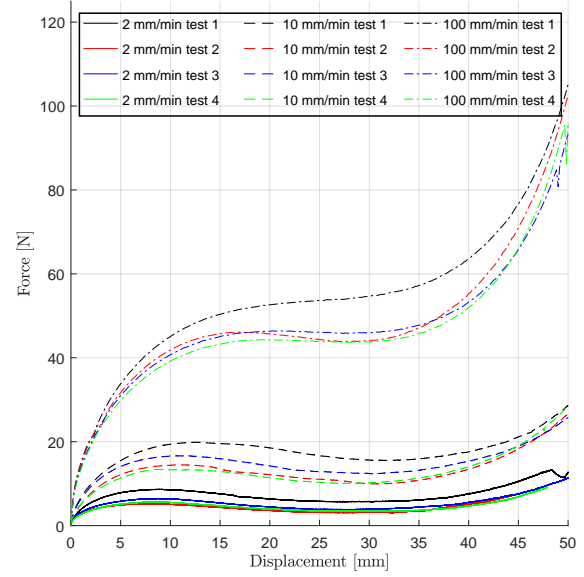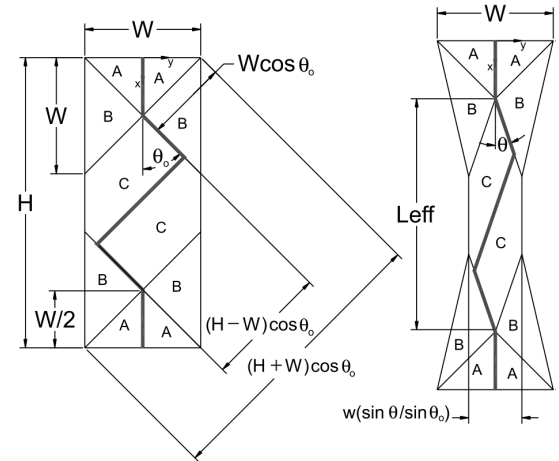$$\gamma = 90° - 2\cos^{-1}\left(\frac{L_0 + \delta}{\sqrt{2}L_0}\right) \tag{8}$$

Figure 10. Kinematics of the bias-extension test [26].

Here the original length of zone C is given as $L_0 = H - W$. Equation (8) assumes that no intra-ply slippage occurs and thus, ideally the shear strain should be measured using e.g. DIC. The shear strain rate is found by differentiating equation (8) w.r.t. time:

$$\dot{\gamma} = \frac{\sqrt{2}}{L_0 \sin\theta}\dot{\delta} \tag{9}$$

So while $\dot{\delta}$ is constant within a test, $\dot{\gamma}$ will increase with increasing shear strain due to $\sin\theta$ entering the equation. In order to obtain constant rate curves, a C^1 continuous interpolated surface of the form $F = F(\gamma, \dot{\gamma})$ is created, where F is the cross head force. One representative set of data from each of the three testing rates (2, 10 and 100 mm/min) are used as input in the interpolation. Now, slices of the surface are taken at the initial strain rates of the tests yielding three constant rate cross head force vs shear angle curves.
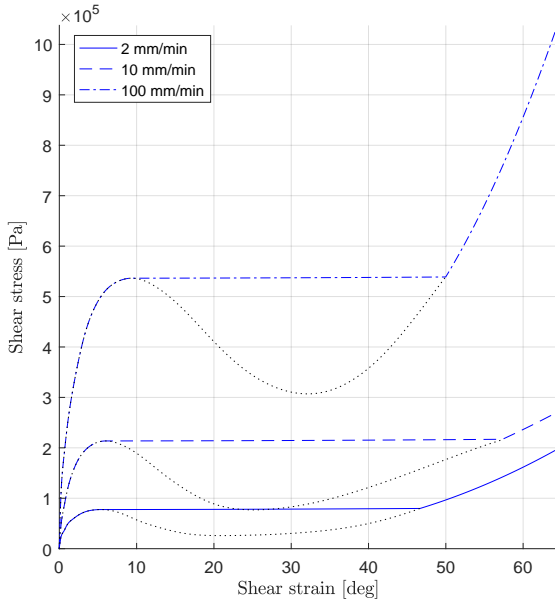
Figure 11. Shear stress vs shear strain for bias-extension tests.

Figure 12. Method to obtain stress-strain curve and strain rate from cantilever test.

Using energy equilibrium the normalized shear force per unit length is derived to[2]:

$$F_{sh}(\gamma) = \frac{1}{(2H - 3W)\cos\gamma} \left[\left(\frac{H}{W} - 1 \right) F \left(\cos\frac{\gamma}{2} - \sin\frac{\gamma}{2} \right) \right.$$
$$\left. - W F_{sh}\left(\frac{\gamma}{2}\right) \cos\frac{\gamma}{2} \right] \qquad (10)$$

Notice how the force evaluated at a shear angle γ depends on the force evaluated at the half shear angle $\frac{\gamma}{2}$. Thus, the expression must be evaluated iteratively. The nominal shear stress τ is found by division with the initial thickness.

A shear stress vs shear angle curve for each cross head rate is presented in Figure 11. In the figure, black dotted lines are drawn in the plateau-region. These lines correspond to the actual calculated shear stresses which are seen to exhibit negative stiffnesses. To avoid instability during the FE solution, the corrected curves with a flat plateau region are used.

In Figure 9 the force drop in the plateau region is also visible. One possible explanation for the drop is relaxation of the material, but this is not investigated further. It must also be pointed out that equation (10) was derived for rate-independent materials. Harrison et al.[27] proposed another formula for rate-dependent materials assuming Newtonian fluid behavior. This approach avoids the negative stiffness, but the Newtonian assumption also introduces errors. Because the material exhibits a rate-dependency, it follows that it has non-Newtonian behavior. In this study, the rate-independent results with negative stiffness correction in Fig. 11 will be used. This decision is made based on Finite Element simulations of the bias-extension test using the two approaches.

Cantilever Test

As introduced previously, the bending behavior of the material model is controlled by the compressive stiffness.
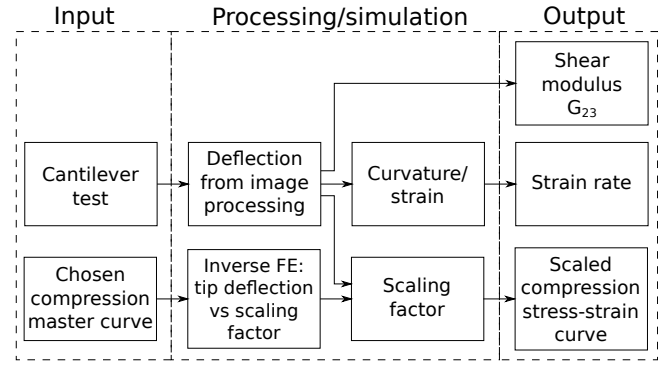
Thus, this section presents the methodology to measure the out-of-plane deformation of the prepreg material and calculate a number of compression stress-strain curves with corresponding strain rates. The end result is introduction of rate-dependent bending in the FE-model. The cantilever test is chosen due to its simple setup and the fact that the loading from gravity is well known. See e.g. Alshahrani and Hojjati[32] for an overview of the various bending test methods.

The basic idea is to capture the deflection of the specimen over time. Based on the deflection, the strain rate as function of time is obtained. Then by using an inverse model approach and the tip deflection of the specimen at different time stamps, compression stress-strain curves are obtained. These steps are outlined in the flowchart in Figure 12 and elaborated in the following.

In the test, the specimen are cut to a width of 25 mm and clamped at one end such that the free length is 150 mm. The free part is held horizontal by a support, which is removed upon start of the test. The experiment is run for 6 minutes until no further deformation is visible. Four samples of 0° and five samples of 90° specimens are tested.

For the data processing, the method used by Liang et al.[33] (see also Dangora et al.[22]) makes up the baseline. It consists of taking a still image of the deflecting specimen, using image processing to extract the midline and fitting a continuous smooth function from which it is possible to obtain the moment-curvature relation. Here, slight modifications are introduced. Instead of still images, a video of the deflecting specimen is recorded whereby the time aspect is taken into account.

The recorded video is handled using MATLAB's Image Processing Toolbox. For each chosen frame, the image is binarized using a global gray level threshold value. Small areas less than some pixel tolerance are removed. Next, the image is eroded, i.e. shrunk to a single pixel in thickness. Practically it is achieved by averaging the nonzero indices for each horizontal coordinate. These steps are depicted in Figure 13. Given the eroded image and the spatial resolution, x and y coordinates of the deflected specimen can be calculated. Next, a polynomial $P(x)$ of order 4 is fitted to the x and y coordinates of the deflected specimen with the constraint that it must pass through the origin.

Using the polynomial, the tip deflection as function of time is found and presented for all the tested specimen in Figure 14. Quite a lot of scatter in the data are observed but it is worth to note that six of the nine recorded deflections
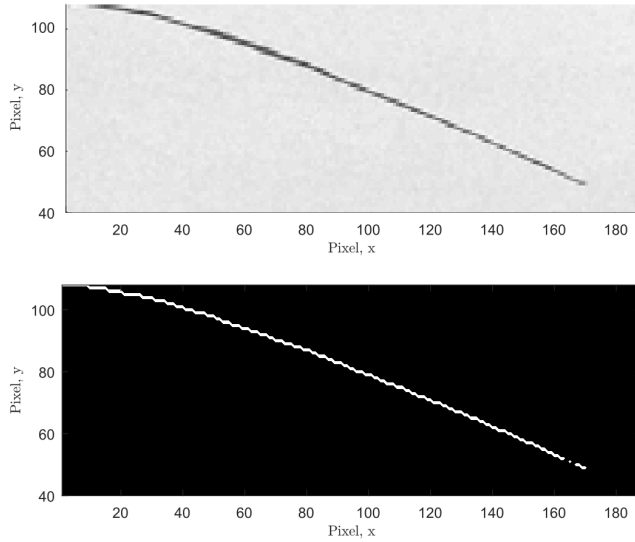
Figure 13. Image processing of cantilever test. Top: grayscale image, bottom: binarized and eroded image.
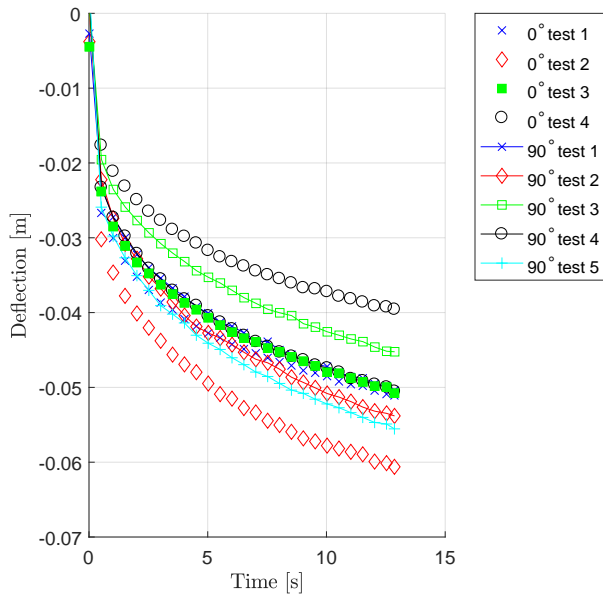

Figure 14. Cantilever tests of 150 mm specimen presented as tip deflection vs time.

are within 5 mm after 13 s. No trends can be seen regarding the orientation of the specimens. Especially the initial conditions, i.e. releasing of the specimen from horizontal is believed to cause the scatter. Other test methods could give better control of the test parameters[32].

In the following, 0° test 3 will be considered since it represents the average behavior of the tests. The curvature of the specimen is found as follows:

$$\kappa = \frac{P''(x)}{\left(1 + P'(x)^2\right)^{\frac{3}{2}}} \tag{11}$$

From which it is possible to calculate the strain using the thickness T of the specimen:

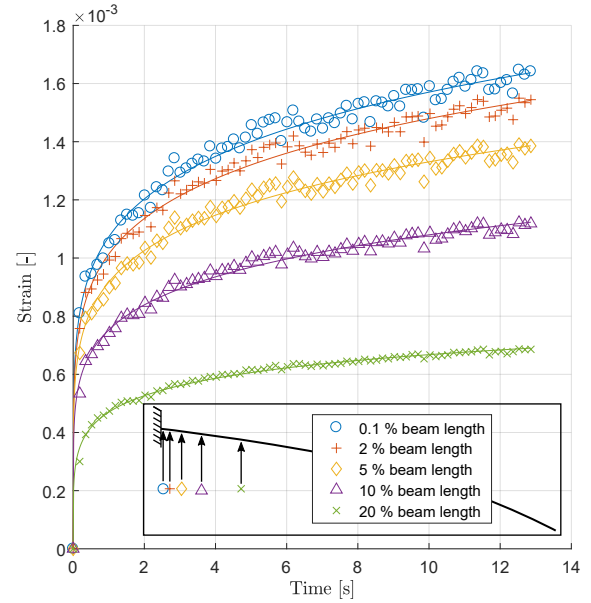$$\varepsilon_{xx} = -0.5\,T\,\kappa \tag{12}$$

Figure 15. Strain vs. time at different percentages of the beam lengths for cantilever specimen.

In this formula it is assumed that the neutral axis is located in the geometric center of the beam. This is not the case when the effective moduli are different in tension and compression. Also the weave style influences the location of the neutral axis. However, since the desired quantity is the *strain rate*, it is believed that the calculation is valid. This is also justified from Figure 15 which depicts the strain vs. time at different percentages of the beam length. The slopes of the curves, i.e. the strain rates, are seen to be very similar over the course of the test, especially near the root end. The solid lines arise from a least squares fit of a double power law on the following form (used for analytical differentiation):

$$\varepsilon_{xx}(t) = at^b + ct^d \tag{13}$$

During the tests it was observed that the specimen mostly deforms near the root end (see also Figure 13). Therefore, the 0.1% beam length curve is used for strain rate calculation for the FE model.

The final information that is derived from the cantilever test is the out-of-plane shear modulus. From Timoshenko beam theory for a linear elastic, small deformation cantilever beam with a uniform load q (gravity) the slope at $x = 0$ is:

$$v'(x = 0) = \frac{qL}{K_s G A} \tag{14}$$

Here K_s is the shear correction factor which, in lack of better, assumes the familiar value of 5/6 for solid homogeneous materials. Based on the root end slope of the experiment, the value of G can be estimated. As expected, it decays with time. In the current FE material model, however, it must be a constant. A value of $G_{13} = G_{23} = 2 \cdot 10^5$ Pa is chosen by manual fitting such that also a physically sensible response is obtained when the ply is subjected to compression.

With the link between the deflection and the strain rate established, the task is now to determine a compression stress-strain curve, that will give the desired deflection. One
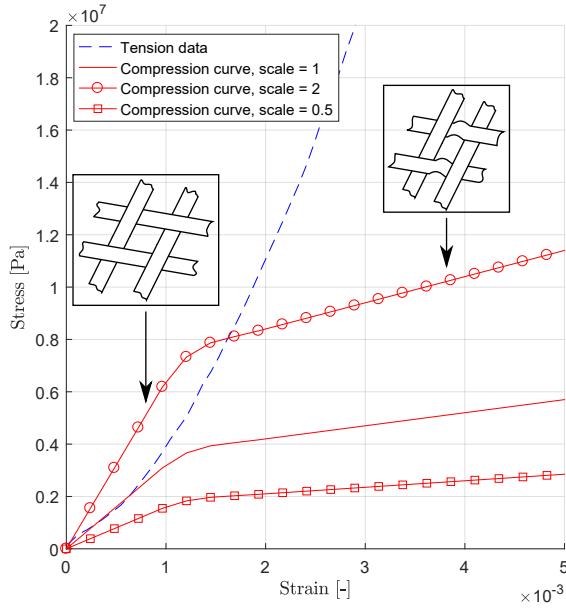
Figure 16. Scalable compression stress-strain curve with break caused by meso-level buckling.

Figure 17. Comparison of experiments and FE simulations of cantilever test. The FE model uses data from *150 mm test 3* as input.

could in principle calculate the moment and then the stress in the beam from beam theory. However, the uncertainty of the neutral axis location in addition to the nonlinear tension response (Figure 8) complicates the operation. Thus, a more robust choice is the inverse model approach.

First, a compression master curve is chosen. The idea is to define the shape of the curve and use a single parameter to scale the curve such that different bending responses are obtained. The chosen master curve resembles a buckling curve where the break of the curve is assumed to arise from meso-level buckling, i.e. buckling of the tows in the unit cell. The curve follows the initial slope of the tension response until 0.1 % strain after which the slope decreases to $5 \cdot 10^8$ Pa. Notice, however, that these slopes were chosen rather arbitrarily. The curve is depicted in Figure 16. A total of 12 FE simulations of a deflecting cantilever beam are then conducted with the compression curve scaled in the range from 0.02 to 10. For each FE simulation the static tip deflection is extracted. Now, interpolating using smooth splines, an expression for the tip deflection of the FE model as function of the scaling factor is obtained.

The only task remaining is to output the desired compression stress-strain curves and corresponding strain rates for the material model. The first curve is generated from data at time equal to 0.4 s in the experiment. The last curve is generated from data where the prepreg specimen has reached a static deflection of 95 mm. Here the strain rate should be effectively zero and is input as $\dot{\varepsilon} = 10^{-15}$. Four curves with equidistant scaling factor are generated in between. Note, that no extrapolation was used in the determination of the stress-strain curves.

Results

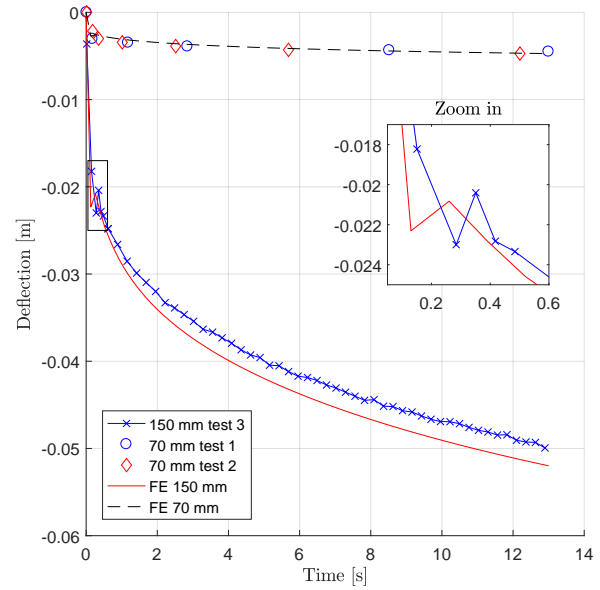This section presents results with the Virtual Draping Environment (VDE).

Simulation of Cantilever Test

As a verification of the cantilever test data processing described in the previous section, two cantilever tests are simulated in Abaqus. This includes a model with the same dimensions as used for the data processing (25 mm × 150 mm) and a shorter model (25 mm × 70 mm). For the latter, two cantilever experiments are conducted for comparison. The results are presented in Fig 17. From the figure it is evident that there is fine agreement between the test and simulation of the 150 mm strip. A small offset of maximum 2 mm or 4 % is seen. For the 70 mm strip there is also good agreement between test and simulation. With the rather large uncertainties of the experiment the bending part of the material model is considered adequate. Regarding the damping, which was described in the section "Transient Nonlinear Finite Element Model", the calculated value is seen to almost critically damp the system. Some initial deflection oscillation is seen in the experimental data and is also captured by the FE simulation as seen in the zoomed-in rectangle. Notice that this is a physical dynamic effect of the test.

Model Validation

In the following, a simple test case with 4 grippers (120 mm spacing) and a 160 mm × 160 mm ply is considered. The ply is draped onto the lower left corner of the test mold (see Figure 3). A test rig where the grippers are controllable in x, y and z directions is used to obtain experimental data. The grippers are mounted in ball joints but no interlinks are used. With these controllable DOF, the system is more deterministic which facilitates the validation. A manually created draping sequence that purposely produces wrinkles is executed and afterwards the draped ply on the mold is recorded using a PrimeSense Carmine 1.09 3D scanner. The same draping sequence is simulated using the transient
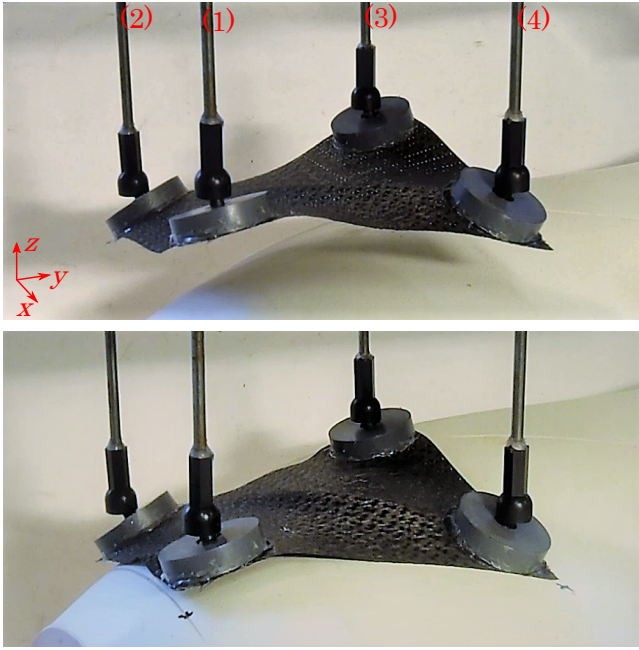
Figure 18. The model validation drape experiment in two different states: Top: After in-plane movement (free hanging). Bottom: Final configuration on the mold.

Figure 19. The model validation FE simulation in two different states: Top: After in-plane movement (free hanging). Bottom: Final configuration on the mold. The colors represent fabric shear strain.

Figure 20. Difference between ply and mold for both experimental (error bars indicate resolution) and FE simulation.

model in Abaqus. The starting position of the grippers is such that they all have the same vertical distance to their target points on the mold surface. The draping sequence consists of two parts: a sequential in-plane movement of three grippers to the x and y coordinates of the target points, followed by a collective vertical movement to the mold surface. To enforce the infinite friction assumption in the model, the grippers (solid nylon discs) are glued onto the ply.

The ply after in-plane deformation and in the final configuration on the mold is depicted in Figure 18. During the in-plane movement of the grippers a large wrinkle is formed in the direction of shearing. This is maintained in the draped configuration. Notice, that this is not due to the fabric reaching the locking angle ($\approx 35°$) since the maximum shearing angle on the mold is about 20° (according to the kinematic mapping algorithm). In addition, because of the mold-ply friction, the grippers are not completely tangent to the mold surface in the final configuration.

The simulation results of the transient FE model are shown in Figure 19 in the same two states (See the appendix for the velocities used). In general, the FE model is seen to predict the tendencies in both states well. The largest discrepancies are seen in the draped configuration near the grippers where also some small penetrations through the mold surface occur. This indicates that the constant Coulomb friction model is a simplification of the actual interface behavior. This may be due to the viscous properties of the prepreg.

Figure 20 presents a plot of the difference between the ply and the mold for both the experiment and the FE model. The data are sampled at a line of constant x-values halfway across the ply. The spatial resolution of the 3D scanner used to record the experimental result is about 0.5 mm which is indicated with error bars in the plot.

The main peak in the plot corresponds to the large diagonal wrinkle, which is predicted well by the FE model. This is mostly related to the material model as the wrinkle
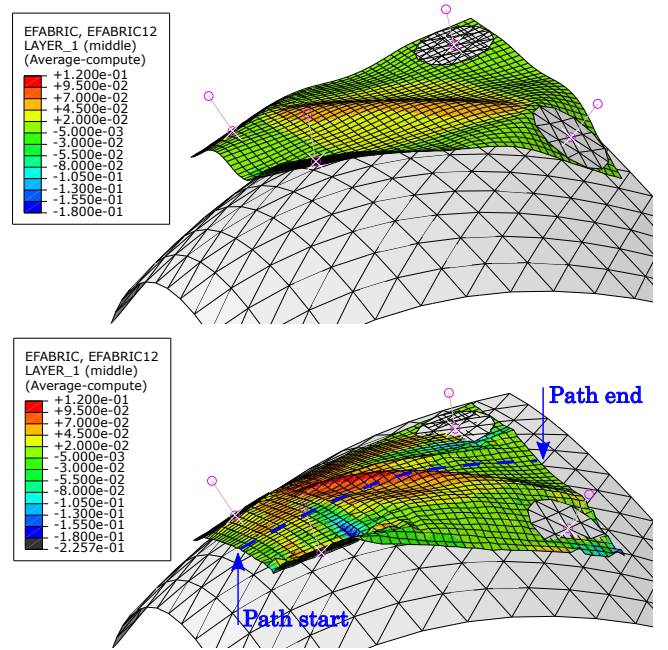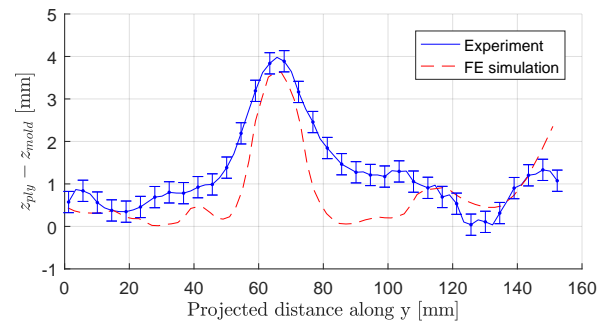
is formed before mold contact as seen in Figure 19. There is a discrepancy of about 1 mm on the right side of the peak at y-distances 80 mm to 110 mm which again is believed to be due to the friction model. At y-distances 110 mm to 160 mm a fair agreement is seen. This wrinkling is partly created before mold contact. Obviously there are a some uncertainties associated with both the FE model and the experiment, so a result of this kind is considered acceptable.

Overall, the comparisons between the FE models and experiments in this and in the previous section indicate that the material model is appropriate while the ply-mold interface model with the simple constant Coulomb friction could be improved. However, the discrepancies in the present example are mostly caused by the grippers when they make contact with the mold at an angle, i.e. they are not tangent to the mold surface. As seen, the friction causes the grippers to halt in these configurations which of course should be avoided already in the planning of the draping sequence. However, as will become evident in the following, the use of interlinks greatly reduces the issue with gripper rotations.
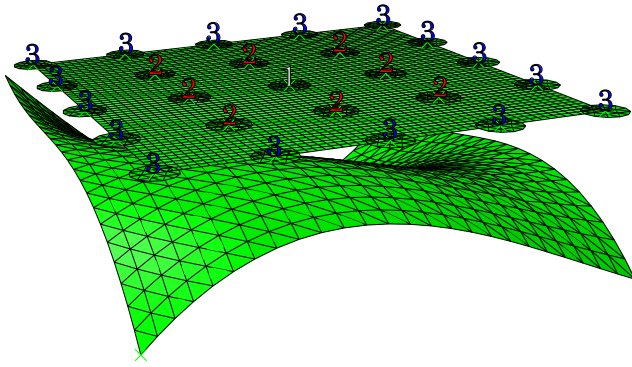
Figure 21. The FE model in the initial configuration. The numbers indicate the groups of grippers in the wave shape draping sequence.
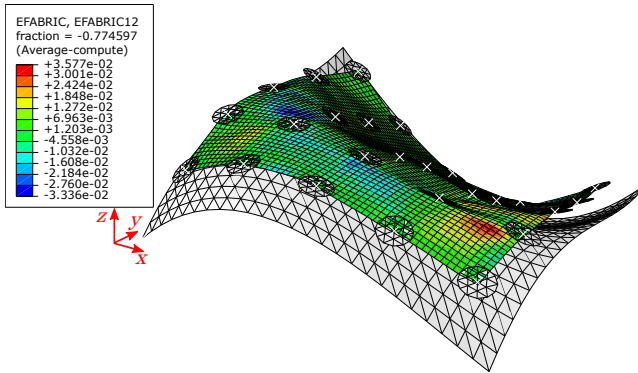

Figure 22. The robot system FE model after preshaping. The colors represent shear strain.

Simulation of Robot System Draping

Consider next a 405 mm × 405 mm ply being draped onto the test mold by the robot system. The interlinks are used in the model and therefore only the z DOF are controllable. The 5 × 5 grid has a spacing of 100 mm. A vertical spring is introduced in the connector elements (see Figure 7) to model the maximum actuator force. This helps prevent mold penetrations since the grippers are displacement controlled. If some grippers are not completely on the mold surface after draping, they will be moved accordingly.

The energy mapping algorithm is used to find the draped configuration. A starting point in the center of the mold is selected and geodesic lines from mid-side to mid-side of the mold edges are created on the mold surface. Since the starting point is in the center of the mold, gripper 3,3, i.e. the one in the center, is fixed in-plane. The initial configuration in the FE model is shown in Figure 21. During draping, the grippers are first moved into the preshape (5 s duration) which is seen in Figure 22. Next, the two different strategies previously outlined in the section "Motion Planning" are executed: The uniform draping sequence and the wave shape draping sequence. Results from both are presented in the following. It is expected that the wave shape draping sequence performs better than the uniform draping sequence because it resembles the current manual operation closer.

Result with Uniform Draping Sequence

As described previously, the uniform draping sequence implicates that all the grippers move towards the mold simultaneously (5 s duration). The result is shown in Fig 23 as a contour plot of the ply-mold difference. The figure shows, that the draped configuration has wrinkles. Especially, the upper left corner has a maximum ply-mold separation of 12.2 mm. The figure also shows the prescribed boundary (red line with circles), i.e. the boundary obtained from the mapping algorithm. Here, it is evident that the upper and lower edges of the ply are far off the boundary - as much as 28 mm in the upper right corner. So while the grippers in principle should make contact with the mold simultaneously using this draping sequence, the steep gradients of the mold in areas with high curvature causes some grippers to make contact with the mold before others. Thereby, some grippers do not reach their target points. From Figure 22 it is seen that the sag of the ply before mold contact is small but even the free-hanging ply can make contact with the mold at the wrong x and y coordinates. Since the in-plane displacements are controlled by the interlinks the error propagates throughout the ply.

Result with Wave Shape Draping Sequence

Next, a wave shape is simulated originating from the center of the mold. The numbers in Figure 21 indicate the order in which the grippers move. Grippers with the same number move to the mold simultaneously in 3.5 seconds. After a delay of 0.8 seconds the next group follows. The last grippers to make contact with the mold are consequently the group 3 grippers. The result is shown in Figure 24. From the figure it is evident that there are still wrinkles in the draped configuration, however, the result is improved compared to the uniform draping sequence. The wrinkles are located in the same areas of the mold but now the maximum ply-mold difference is reduced to 10.1 mm (12.2 mm previously) and the boundary offset of the upper right corner is reduced to about 20 mm (28 mm previously). The middle part of the ply from where the wave originates as well as the lower left corner is now completely free from wrinkles. Thus, the wave shape draping sequence is an improvement but the issues in the areas of high mold curvature as described in the previous section persist. A 3D view of the draped configuration is presented in Figure 25.

Please note, that both of the results presented in Figures 23 and 24 are inconsistent with the requirements of no wrinkles and placement within the boundary and thus cannot be accepted in an industrial context.

Conclusions

This paper has introduced a Virtual Draping Environment (VDE) for planing and simulating draping sequences for the robot system under development. The z-velocity of each gripper in the array must be determined such that the draped configuration is free from wrinkles. Here, the emphasis has been on setting up the transient non-linear Finite Element (FE) model and using it for simulation of the draping process. To this end, material characterization was employed which consists of tension tests, bias-extension tests, and cantilever tests. Especially the shear and bending response showed a high degree of rate-dependency. This was expected since the ply is a prepreg.
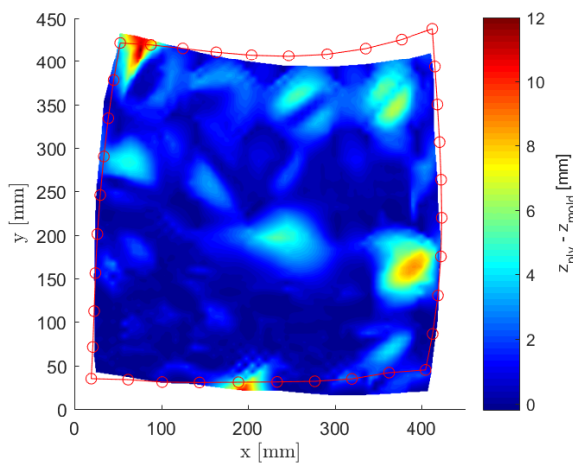
Figure 23. Contour plot of ply-mold difference for uniform draping sequence. The red line with circles indicates the prescribed boundary.
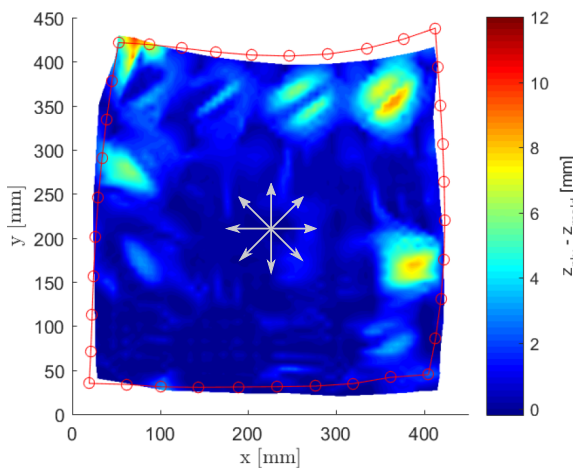

Figure 24. Contour plot of ply-mold difference for wave shape draping sequence. The red line with circles indicates the prescribed boundary. The arrows show the wave direction.
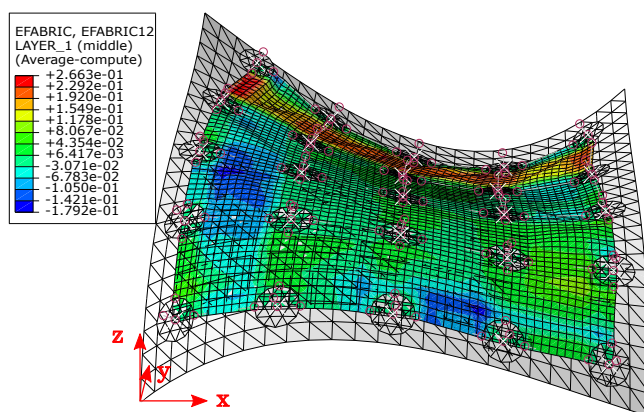

Figure 25. The draped configuration of the wave shape draping sequence. The colors indicate fabric shear strain.

The bending response of the FE model is achieved by adjusting the compressive stiffness in the fiber direction. By means of video recording of the cantilever test and image processing, the experimental deflection was determined. Additionally, the strain rate was calculated in order to include the rate-dependency in the FE model. Using an

inverse modeling approach, the bending response of the FE model was adjusted to match that of a cantilever test. This approach showed good agreement - also when comparing to a cantilever test of a shorter specimen.

To test the FE model in its entirety, a simple 4-gripper experimental arrangement was used. When comparing the subsequent FE simulation with the experiment, the material model seemed to be appropriate while the simple Coulomb friction interface could be improved. It was, however, noted that the lack of interlinks (see Figure 2) in the validation setup caused some particular difficult interface conditions which are avoided when simulating the robot drape tool.

Finally, the FE model was used to evaluate two different gripper move patterns or *draping strategies*. The first was a uniform strategy where all grippers move towards the mold simultaneously. The second is a wave shape strategy where grippers move in a droplet or wave originating from the center of the mold. Both of the simulated draping sequences resulted in wrinkles but the wave shape strategy performed slightly better.

To this end it is interesting to note that both simulations used the same z-displacements of the grippers but executed in different ways. The grippers do not terminate at the same locations in the two simulations so it cannot directly be concluded that it is a path dependent problem. However, the fact that the differences result from mold-ply friction which itself is a path dependent phenomenon and that wrinkles can be formed already in the free hanging configuration (see Figure 18) is strong evidence.

The work presented in this paper is only a small step towards modeling of automated manipulation of prepregs. The griper-ply interface which was neglected in this study, should be investigated carefully. Although the frictional resistance appears high, it should be checked that it is sufficient when the ply is sheared. The current tie contact probably also overconstrains the ply which could lead to unphysical wrinkling. Feasible draping sequences where the ply border matches the prescribed boundary should be generated. To this end it could be interesting to investigate whether optimization techniques can be employed. Wrinkles should also be avoided but another approach would be to investigate what wrinkle sizes and shapes that can be removed during debulking of the layup.

By continuing the study of robotic draping it is hoped that the cost of carbon fiber parts for the aerospace industry eventually can be lowered.

Declaration of conflicting interests

The Authors declare that there is no conflict of interest.

Funding

References

1. Lukaszewicz D, Ward C and Potter KD. The engineering aspects of automated prepreg layup: History, present and

future. *Composites Part B: Engineering* 2012; 43(3): 997–1009. DOI:10.1016/j.compositesb.2011.12.003.

2. Cao J, Akkerman R, Boisse P et al. Characterization of mechanical behavior of woven fabrics: Experimental methods and benchmark results. *Composites Part A: Applied Science and Manufacturing* 2008; 39(6): 1037–1053. DOI:10.1016/j.compositesa.2008.02.016.

3. Boisse P, Hamila N, Vidal-Salle E et al. Simulation of wrinkling during textile composite reinforcement forming. Influence of tensile, in-plane shear and bending stiffnesses. *Composites Science and Technology* 2011; 71(5): 683–692. DOI:10.1016/j.compscitech.2011.01.011.

4. Womersley JR. 6.THE APPLICATION OF DIFFERENTIAL GEOMETRY TO THE STUDY OF THE DEFORMATION OF CLOTH UNDER STRESS. *Journal of the Textile Institute Transactions* 1937; 28(3): T97–T113. DOI:10.1080/19447023708658810.

5. Mack C and Taylor HM. The Fitting of Woven Cloth to Surfaces. *Journal of the Textile Institute Transactions* 1956; 47(9): T477–T488. DOI:10.1080/19447027.1956.10750433.

6. Aimene Y, Vidal-Salle E, Hagege B et al. A Hyperelastic Approach for Composite Reinforcement Large Deformation Analysis. *Journal of Composite Materials* 2010; 44(1): 5–26. DOI:10.1177/0021998309345348.

7. Peng X, Guo Z, Du T et al. A simple anisotropic hyperelastic constitutive model for textile fabrics with application to forming simulation. *Composites Part B: Engineering* 2013; 52: 275–281. DOI:10.1016/j.compositesb.2013.04.014.

8. Yu W, Pourboghrat F, Chung K et al. Non-orthogonal constitutive equation for woven fabric reinforced thermoplastic composites. *Composites Part A: Applied Science and Manufacturing* 2002; 33(8): 1095–1105. DOI:10.1016/S1359-835X(02)00053-2.

9. Skordos AA, Monroy Aceves C and Sutcliffe MPF. A simplified rate dependent model of forming and wrinkling of pre-impregnated woven composites. *Composites Part A: Applied Science and Manufacturing* 2007; 38(5): 1318–1330. DOI:10.1016/j.compositesa.2006.11.005.

10. Jauffrès D, Sherwood JA, Morris CD et al. Discrete mesoscopic modeling for the simulation of woven-fabric reinforcement forming. *International Journal of Material Forming* 2010; 3(SUPPL. 2): 1205–1216. DOI:10.1007/s12289-009-0646-y.

11. Harrison P. Modelling the forming mechanics of engineering fabrics using a mutually constrained pantographic beam and membrane mesh. *Composites Part A: Applied Science and Manufacturing* 2016; 81: 145–157. DOI:10.1016/j.compositesa.2015.11.005.

12. Cherouat A and Billoët JL. Mechanical and numerical modelling of composite manufacturing processes deep-drawing and laying-up of thin pre-impregnated woven fabrics. *Journal of Materials Processing Technology* 2001; 118(1-3): 460–471. DOI:10.1016/S0924-0136(01)00987-6.

13. Hamila N, Boisse P and Chatel S. Semi-discrete shell finite elements for textile composite forming simulation. *International Journal of Material Forming* 2009; 2(SUPPL. 1): 169–172. DOI:10.1007/s12289-009-0518-5.

14. Lin H, Clifford M, Taylor P et al. 3D mathematical modelling for robotic pick up of textile composites. *Composites Part B: Engineering* 2009; 40(8): 705–713. DOI:10.1016/j.compositesb.2009.07.006.

15. Bergsma OK and Huisman J. Deep drawing of fabric reinforced thermoplastics. In Brebbia CA, de Wilde WP and Blain WR (eds.) *Computer aided design in composite material technology*. Springer-Verlag, Berlin, pp. 323–334.

16. Van Der Weeën F. Algorithms for draping fabrics on doubly-curved surfaces. *International Journal for Numerical Methods in Engineering* 1991; 31(7): 1415–1426. DOI:10.1002/nme.1620310712.

17. Laroche D and Vu-Khanh T. Forming of Woven Fabric Composites. *Journal of Composite Materials* 1994; 28(18): 1825–1839.

18. Hancock SG and Potter KD. The use of kinematic drape modelling to inform the hand lay-up of complex composite components using woven reinforcements. *Composites Part A: Applied Science and Manufacturing* 2006; 37(3): 413–422. DOI:10.1016/j.compositesa.2005.05.044.

19. Dassault Systèmes Simulia Corporation. Abaqus 6.14 Documentation: 23.4.1 Fabric material behavior, 2014.

20. Döbrich O, Gereke T, Diestel O et al. Decoupling the bending behavior and the membrane properties of finite shell elements for a correct description of the mechanical behavior of textiles with a laminate formulation. *Journal of Industrial Textiles* 2014; 44(1): 70–84. DOI:10.1177/1528083713477442.

21. Yu W, Zampaloni M, Pourboghrat F et al. Analysis of flexible bending behavior of woven preform using non-orthogonal constitutive equation. *Composites Part A: Applied Science and Manufacturing* 2005; 36(6): 839–850. DOI:10.1016/j.compositesa.2004.10.026.

22. Dangora LM, Mitchell CJ and Sherwood JA. Predictive model for the detection of out-of-plane defects formed during textile-composite manufacture. *Composites Part A: Applied Science and Manufacturing* 2015; 78: 102–112. DOI:10.1016/j.compositesa.2015.07.011.

23. Cook R, Malkus DS and Plesha ME. *Concepts and applications of finite element analysis*. New York: John Wiley & Sons, Inc., 2002. ISBN 8126513365.

24. Willems A, Lomov SV, Verpoest I et al. Drape-ability characterization of textile composite reinforcements using digital image correlation. *Optics and Lasers in Engineering* 2009; 47(3-4): 343–351. DOI:10.1016/j.optlaseng.2008.03.012.

25. Zhu B, Yu T, Teng J et al. Theoretical Modeling of Large Shear Deformation and Wrinkling of Plain Woven Composite. *Journal of Composite Materials* 2008; 43(2): 125–138. DOI:10.1177/0021998308098237.

26. Lebrun G, Bureau MN and Denault J. Evaluation of bias-extension and picture-frame test methods for the measurement of intraply shear properties of PP/glass commingled fabrics. *Composite Structures* 2003; 61(4): 341–352. DOI:10.1016/S0263-8223(03)00057-6.

27. Harrison P, Clifford M and Long A. Shear characterisation of viscous woven textile composites: A comparison between picture frame and bias extension experiments. *Composites Science and Technology* 2004; 64(10-11): 1453–1465. DOI:10.1016/j.compscitech.2003.10.015.

28. Grosberg P and Park BJ. The Mechanical Properties of Woven Fabrics: Part V: The Initial Modulus and the Frictional Restraint in shearing of Plain Weave Fabrics. *Textile Research Journal* 1966; 36(5): 420–431. DOI:10.1177/004051756603600505.

29. Nguyen M, Herszberg I and Paton R. The shear properties of woven carbon fabric. *Composite Structures* 1999; 47(1-4): 767–779. DOI:10.1016/S0263-8223(00)00051-9.

30. Boisse P, Hamila N, Guzman-Maldonado E et al. The bias-extension test for the analysis of in-plane shear properties of textile composite reinforcements and prepregs: a review. *International Journal of Material Forming* 2017; 10(4): 473–492. DOI:10.1007/s12289-016-1294-7.

31. Harrison P, Tan MK and Long AC. Kinematics of Intra-Ply Slip in Textile Composites during Bias Extension Tests. In *8th Int. ESAFORM Conf. on Materials Forming*. pp. 987–990.

32. Alshahrani H and Hojjati M. A new test method for the characterization of the bending behavior of textile prepregs. *Composites Part A: Applied Science and Manufacturing* 2017; 97: 128–140. DOI:10.1016/j.compositesa.2017.02.027.

33. Liang B, Chaudet P and Boisse P. Curvature determination in the bending test of continuous fibre reinforcements. *Strain* 2017; 53(1): e12213. DOI:10.1111/str.12213.

Appendix: 4-Gripper FE Prescribed Velocities

Table 1 presents the 4-gripper FE model velocity boundary conditions, which were obtained from the grippers in the experiment. The initial coordinate of gripper 2 is $\{39.8, 40.1, 137.0\}$ mm with the other grippers placed such that they form a square grid with side lengths 120 mm.

Table 1. Velocities prescribed in the 4-gripper FE model. Non-active grippers are prescribed a zero velocity.

Step	Grp.		Velocity [mm/s]			Time [s]
1	1	{	0.0,	0.0,	-0.93 }	3
1	2	{	0.0,	0.0,	-9.53 }	3
1	4	{	0.0,	0.0,	-4.27 }	3
2	1	{	-2.9,	4.0,	0.0 }	2
3	3	{	4.1,	-0.22,	0.0 }	2
4	4	{	0.67,	0.74,	0.0 }	18
5	1,2,3,4	{	0.0,	0.0,	-5.1 }	6
6	1	{	-1.0,	-3.0,	0.0 }	1
6	2	{	-0.75,	-0.75,	0.0 }	1
6	3	{	-1.0,	1.0,	0.0 }	1
6	4	{	-2.0,	-3.0,	0.0 }	1